

Amplitudes and Observables in pp Elastic Scattering

at $\sqrt{s} = 7$ TeV

A. K. Kohara, E. Ferreira, and T. Kodama

Instituto de Física, Universidade Federal do Rio de Janeiro

C.P. 68528, Rio de Janeiro 21945-970, RJ, Brazil

Abstract

A precise analysis of the pp elastic scattering data at 7 TeV in terms of its amplitudes is performed as an extension of previous studies for lower energies. Slopes B_R and B_I of the real and imaginary amplitudes are independent quantities, and a proper expression for the Coulomb phase is derived. The real and imaginary amplitudes are fully disentangled, consistently with forward dispersion relations for amplitudes and for slopes. We present analytic expressions for the amplitudes that cover all t range completely, while values of total cross section σ , ratio ρ , B_I and B_R enter consistently to describe forward scattering. It is stressed that the identification of the amplitudes is an essential step for the description of elastic scattering, and pointed out the importance of the experimental investigation of the transition range from non-perturbative to perturbative dynamics, that may confirm the three gluon exchange mechanism observed at lower energies.

I. INTRODUCTION

The determination of the imaginary and real parts of the amplitudes of elastic pp and $p\bar{p}$ scattering is an essential step for the understanding of the underlying dynamics governing hadronic interactions and for the construction and critical evaluation of theoretical models. This question has now increased renewed interest in view of the experimental activity at new energy frontiers of LHC, particularly with the forward physics measurements of the TOTEM Collaboration [1, 2], and also with the possibility of measurements in the large $|t|$ range. However, the identification of amplitudes is not at all a trivial task. There is no methodology completely free from subjective judgment and of interpolations and extrapolations based on investigation of data at all energies.

Efforts to identify amplitudes were made in a treatment originated in the Stochastic Vacuum Model [3], resulting in good description of the data on $d\sigma/dt$ at all energies from 20 to 1800 GeV [4]. In particular, it was made clear to establish the regularity in the general features of the real and imaginary amplitudes, by identifying their magnitudes, signs and zeros of the individual parts.

The constraints imposed by the well-known dispersion relations for the amplitudes and also by the new dispersion relations for the slopes [5] help to control the forward scattering parameters, and are essential tool for the construction of valid analytic representations of the data. In the present work, we extend the previous analysis to the recent pp elastic scattering measurements of the LHC TOTEM Collaboration [1, 2] at $\sqrt{s} = 7$ TeV, obtaining a very precise description of the amplitudes and of the differential cross section in the whole $|t|$ range, including location, depth and shape of dip and bump. The quantities σ , ρ and slopes B_I and B_R that are the common parameters of the basic features of the forward scattering data, are also determined precisely from this all- t analysis. Furthermore, we show that the 7 TeV data favor the assumption of universality of the contribution from the perturbative three gluon exchange process at large $|t|$ that has been observed at 27.4 GeV [6] and confirmed at higher ISR energies.

Our analysis shows why the dip/bump or inflection structure, that appears in pp and $p\bar{p}$ elastic differential cross section at ISR and Tevatron energies, has also been observed at 7 TeV [1, 2]. This is due to the monotonic displacement of the zero of the

imaginary part as the incident energy increases, approaching the first zero of the real amplitude, with formation of a marked dip at about 0.5 GeV^2 . We remark that at the energies 540 and 1800 GeV no dip-bump appears because the imaginary zero is in the middle between the two zeros of the real part, with compensating contributions. This analysis also suggests that, mainly as consequence of the continued displacement of the zero of the imaginary part, an even more pronounced dip/bump structure should appear for 14 TeV pp scattering at a slightly smaller value $|t| \simeq 0.4 \text{ GeV}^2$.

We organize the present paper as follows. In Sec. II, we introduce the representation of our amplitudes. This representation contains the exponential nature of the very forward domain, with associated Coulomb amplitude and phase, and the larger $|t|$ behavior with dip and bump, together with the contribution from the perturbative three-gluon exchange process, all in unique analytic forms. We also show the form of the nuclear amplitude in impact parameter space, originated in studies with the Stochastic Vacuum Model. In Sec. III we show our results for the scattering amplitudes obtained from a precise fit to the experimental data at 7 TeV. It is shown that the forward scattering parameters determined from our analytic expression for all t values are in agreement with those determined by the TOTEM collaboration [2]. In Sec. IV we discuss the physical nature of the amplitudes, the position of zeros and its relation to the observed dip/bump structure. These properties are compared to the case of 52.8 GeV, where a wider t domain has been measured. To make clear the physical meaning of the properties of the amplitudes, a short comparison with other model has been done. Finally in Sec. V we give a summary of the present work, and discuss the consequences of our analysis, together with the future perspectives. In Appendix, we derive the Coulomb phase function extended to deal with the case of different slopes B_I and B_R .

II. ANALYTIC REPRESENTATION OF AMPLITUDES OF pp ELASTIC SCATTERING

We write the differential cross section as

$$\frac{d\sigma}{dt} = (\hbar c)^2 |T_R(s, t) + iT_I(s, t)|^2. \quad (2.1)$$

In the following discussion, we use the unit system where σ is in mb (millibarns) and the energy in GeV, so that $(\hbar c)^2 = 0.3894 \text{ mb GeV}^2$.

T_R and T_I , with dimensions GeV^{-1} , contain the nuclear and the Coulomb parts in the forms

$$T_R(s, t) = T_R^N(s, t) + \sqrt{\pi} F^C(t) \cos(\alpha\Phi) , \quad (2.2)$$

and

$$T_I(s, t) = T_I^N(s, t) + \sqrt{\pi} F^C(t) \sin(\alpha\Phi) . \quad (2.3)$$

The Coulomb scattering amplitude $F^C(s, t)$ enters in the pp/pp̄ amplitudes with the form

$$F^C(t) e^{i\alpha\Phi(s, t)} = (-/+) \frac{2\alpha}{|t|} F_{\text{proton}}^2(t) e^{i\alpha\Phi(s, t)} , \quad (2.4)$$

where α is the fine-structure constant, $\Phi(s, t)$ is the Coulomb phase and the proton form factor is written

$$F_{\text{proton}}(t) = [0.71/(0.71 + |t|)]^2 . \quad (2.5)$$

The total cross section is given by

$$\sigma = 4\sqrt{\pi} (\hbar c)^2 T_I^N(s, t=0) . \quad (2.6)$$

$T_R^N(s, t)$ and $T_I^N(s, t)$, respectively the real and imaginary parts of the properly normalized scattering amplitude of the strong interaction, are smooth and regular functions of s and t , and the Coulomb amplitude is relevant in the very forward range $|t| < 10^{-2} \text{ GeV}^2$. We neglect spin effects.

A. Nuclear Amplitudes for all- t Values

To obtain precise description of the elastic $d\sigma/dt$ data for all $|t|$, we use the forms that have been introduced before and shown to be successful with ISR and Fermilab data [4], together with the assumption of the perturbative three-gluon exchange amplitude [7], writing

$$T_K^N(s, t) = \alpha_K(s) e^{-\beta_K(s)|t|} + \lambda_K(s) \Psi_K(\gamma_K(s), t) + \delta_{K,R} R_{ggg}(t) , \quad (2.7)$$

where $\Psi_K(\gamma_K(s), t)$ are shape functions, described below, and $R_{ggg}(t)$ represents the contribution from the perturbative three-gluon exchange amplitude. The label K

means either $K = R$ for the real amplitude or $K = I$ for the imaginary amplitude, and $\delta_{K,R}$ is the Kronecker's delta symbol, that is, the last term only contributes for the real part.

1. Shape functions

The shape functions are written

$$\Psi_K(\gamma_K(s), t) = 2 e^{\gamma_K} \left[\frac{e^{-\gamma_K \sqrt{1+a_0|t|}}}{\sqrt{1+a_0|t|}} - e^{\gamma_K} \frac{e^{-\gamma_K \sqrt{4+a_0|t|}}}{\sqrt{4+a_0|t|}} \right], \quad (2.8)$$

with the property $\Psi_K(\gamma_K(s), t = 0) = 1$. We here introduced for each amplitude 4 energy dependent parameters, α_K , β_K , γ_K , λ_K , whose roles are explained below. γ_K is dimensionless, while α_K , γ_K and β_K are in GeV^{-2} . The fixed quantity $a_0 = 1.39 \text{ GeV}^{-2}$ is related to the square of the correlation length a of the gluon vacuum expectation value, with $a = (0.2 \sim 0.3) \text{ fm}$ [3].

These forms for the amplitudes originate in a formulation of pp scattering in impact parameter b space in studies based on the Stochastic Vacuum Model [3, 4]. The analytic representation of our nuclear amplitude (except for the perturbative three-gluon exchange contribution) has a simpler form in terms of impact parameter space through the Fourier transforms,

$$\tilde{T}_K(s, b) = \frac{1}{2\pi} \int d^2\vec{q} e^{-i\vec{q}\cdot\vec{b}} T_K^N(s, t = -q^2),$$

which are given in closed forms as

$$\tilde{T}_K(s, b) = \frac{\alpha_K}{2 \beta_K} e^{-\frac{b^2}{4\beta_K}} + \lambda_K \tilde{\psi}_K(s, b), \quad (2.9)$$

where

$$\tilde{\psi}_K(s, b) = \frac{2 e^{\gamma_K}}{a_0} \frac{e^{-\sqrt{\gamma_K^2 + \frac{b^2}{a_0}}}}{\sqrt{\gamma_K^2 + \frac{b^2}{a_0}}} \left[1 - e^{\gamma_K} e^{-\sqrt{\gamma_K^2 + \frac{b^2}{a_0}}} \right] \quad (2.10)$$

is the shape function in b space. More details of the representation of amplitudes in b -space are given in Sec. IV. We here choose to work with the amplitudes in t -space because they are more directly connected to the $d\sigma/dt$ data that we intend to describe.

These expressions are planned to represent the non - perturbative dynamics of scattering for all $|t|$ and the perturbative term R_{ggg} is tuned to vanish for small $|t|$.

The limits at $|t| = 0$ lead to the values for the total cross section σ , the ratio ρ of the real to imaginary amplitudes, and the slopes $B_{R,I}$ at $t = 0$ through

$$\sigma(s) = 4\sqrt{\pi} (\hbar c)^2 (\alpha_I(s) + \lambda_I(s)) , \quad (2.11)$$

$$\rho(s) = \frac{T_R^N(s, t=0)}{T_I^N(s, t=0)} = \frac{\alpha_R(s) + \lambda_R(s)}{\alpha_I(s) + \lambda_I(s)} , \quad (2.12)$$

$$B_K(s) = \frac{1}{T_K^N(s, t)} \frac{dT_K^N(s, t)}{dt} \Big|_{t=0} = \frac{1}{\alpha_K(s) + \lambda_K(s)} \times \left[\alpha_K(s)\beta_K(s) + \frac{1}{8}\lambda_K(s)a_0(6\gamma_K(s) + 7) \right] . \quad (2.13)$$

The determination of each amplitude starts with four energy dependent parameters that must be obtained from the data. However, with well established s dependences of the imaginary slope B_I (with typical Regge model behavior), connections between $\lambda_R + \alpha_R$ and $\lambda_I + \alpha_I$, plus constraints from dispersion relation for slopes [5], in practice we deal with less independent parameters to describe $d\sigma/dt$ at each energy.

As discussed before [4], the shape functions in Eq. (2.8) are very convenient choices for all values of $|t|$, determining consistently for all energies the zeros, the formation of dips and bumps, the signs and magnitudes of the two amplitudes and are able to reproduce with good accuracy all $d\sigma/dt$ behavior. This description represents the non-perturbative QCD dynamics that is responsible for soft elastic hadronic scattering. They account effectively for the terms of Regge and/or eikonal phenomenology that determine the process for $|t|$ ranges up to about $|t| \approx 2.5 \text{ GeV}^2$. For higher $|t|$, perturbative contributions may become important.

2. Universal behavior at large $|t|$: Faissler measurements at 27.4 GeV

For $|t|$ values beyond the dip and bump characteristic of the differential cross sections at ISR/CERN and Fermilab energies, namely for $|t| > 1.5 \text{ GeV}^2$, the differential cross sections become increasingly independent of the energy. The measurements of pp scattering at $\sqrt{s} = 27.4 \text{ GeV}$ [6] provides the only large $|t|$ data, covering the interval from 5.5 to 14.2 GeV^2 . It is known that the points are smoothly and naturally connected with the lower $|t|$ points at all energies [4]. As shown by Donnachie and Landshoff [7] this tail corresponds to a perturbative three-gluon exchange mechanism, with real amplitude positive for pp and negative for $p\bar{p}$ scattering, and $d\sigma/dt$

falling as $|t|^{-8}$. The most remarkable example is given by the data of pp scattering at $\sqrt{s} = 52.8$ GeV [8], with measurements up to $|t| = 9.75$ GeV² that superpose well with the 27.4 GeV tail. This indicates that in this region the non-perturbative real part is indeed positive, and also that the magnitude of the imaginary part is small compared to the real part. At high energies in p \bar{p} scattering the negative sign of the perturbative tail may lead to a marked dip in the transition region from 3 to 4 GeV².

Based on this expectation for the perturbative tail, we introduce a simple form of the universal three-gluon contribution amplitude $R_{ggg}(t)$ at large $|t|$, parameterizing the Landshoff term of the amplitude as

$$R_{ggg}(t) \equiv \pm 0.45 t^{-4} (1 - e^{-0.005|t|^4}) (1 - e^{-0.1|t|^2}) , \quad (2.14)$$

where the last two factors cut-off this term smoothly in the non-perturbative domain, and the signs \pm refer to the pp and p \bar{p} amplitudes respectively.

Although the cut-off factors written in Eq. (2.14) have been adequate for all cases that were examined, their detailed forms in the transition range ($2.5 < |t| < 4$) GeV² must be examined with data.

B. Exponential forms of amplitudes for very small $|t|$

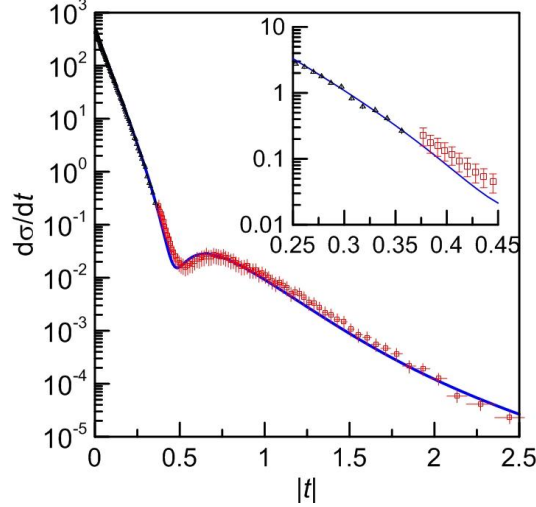
In the treatment of elastic pp and p \bar{p} scattering in the forward direction, with amplitudes approximated by pure exponential forms, the differential cross section is written

$$\begin{aligned} \frac{d\sigma}{dt} = \pi (\hbar c)^2 \bigg\{ & \left[\frac{\rho\sigma}{4\pi(\hbar c)^2} e^{B_R t/2} + F^C(t) \cos(\alpha\Phi) \right]^2 \\ & + \left[\frac{\sigma}{4\pi(\hbar c)^2} e^{B_I t/2} + F^C(t) \sin(\alpha\Phi) \right]^2 \bigg\} , \end{aligned} \quad (2.15)$$

where $t \equiv -|t|$ and we account for different values for the slopes B_I and B_R of the imaginary and real amplitudes. The expression for the Coulomb phase that accounts for $B_R \neq B_I$ derived in the Appendix.

In elastic pp and p \bar{p} scattering at all energies above $\sqrt{s} = 19$ GeV, the real and imaginary amplitudes have zeros located in ranges $|t| \approx (0.1 \sim 0.3)$ GeV² and $|t| = (0.5 \sim 1.5)$ GeV² respectively, and the use of exponential forms beyond a limited forward range could lead to inaccurate determination of the characteristic

FIG. 1: Analytic representation for the data on $d\sigma/dt$ for elastic pp scattering at 7 TeV, together with the experimental data [2]; triangles are for subset A and open squares for subset B . The values of the parameters are given in Eqs. (3.1), (3.2). The inset at the up-right corner shows in closeup a gap between the datasets A and B , that seems to be at the limit of the error bars.



forward scattering parameters σ , ρ , B_I and B_R . We then need to use more general expressions that are connected with the exponential behavior as limits, such as the forms with shape functions written in Eqs. (2.7), (2.8).

III. DATA ON pp SCATTERING AT 7 TEV

A. Determination of Amplitude Parameters

The TOTEM Collaboration has published data of differential elastic cross section [2] in two separate tables, in the ranges $0.00515 \leq |t| \leq 0.371$ (referred to as dataset A) and $0.377 \leq |t| \leq 2.443$ (referred to as dataset B) GeV^2 , with 87 and 78 points respectively. Rather large systematic errors are informed in the dataset B . The representation of these data with the analytical forms of Eqs. (2.7) and (2.8) is shown in Fig. 1. The averaged square deviation for the datasets $A + B$ (165 points) is $\langle \chi^2 \rangle = 0.3105$. The values of the quantities that also enter in the forward scattering amplitudes treated with exponential functions as in Eq. (2.15) are

$$\begin{aligned} \sigma &= 98.65 \pm 0.26 \text{ mb} , \quad \rho = 0.141 \pm 0.001 , \\ B_I &= 19.77 \pm 0.03 \text{ GeV}^{-2} , \quad B_R = 30.2 \pm 0.7 \text{ GeV}^{-2} , \end{aligned} \quad (3.1)$$

FIG. 2: Data for elastic pp scattering at 7 TeV ([2], 165 points) and 52.8 GeV ([8], 97 points). The lines represent the parameterizations with Eqs. (2.7) and (2.8), with average squared deviations $\langle\chi^2\rangle = 0.3105$ and 0.8328 respectively. Numerical characteristic values and description of features of the data and of the amplitudes are given in the text and in Tables I and II .

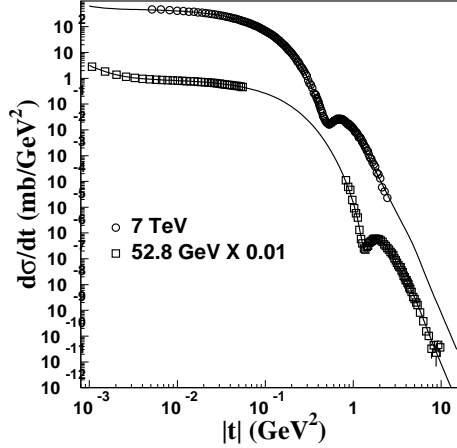


TABLE I: Amplitude parameters for the 52.8 GeV and 7 TeV data.

\sqrt{s} GeV	N points	σ mb	ρ –	B_I GeV $^{-2}$	B_R GeV $^{-2}$	α_I GeV $^{-2}$	β_I GeV $^{-2}$	λ_R GeV $^{-2}$	β_R GeV $^{-2}$	$\langle\chi^2\rangle$
52.8	97	42.49	0.078	13.04	19.07	5.9561	2.3477	1.1307	1.1436	0.8328
7000	165	98.65	0.141	19.77	30.20	13.730	4.0826	4.7525	1.4851	0.3105

and the other independent quantities that enter in the full- t forms are (in GeV $^{-2}$)

$$\begin{aligned}\alpha_I &= 13.730 \pm 0.030 , \quad \beta_I = 4.0826 \pm 0.0093 , \\ \lambda_R &= 4.7525 \pm 0.0155 , \quad \beta_R = 1.4851 \pm 0.0318 .\end{aligned}\tag{3.2}$$

Here we have 8 independent values, that are collected in Table I. [22] Other quantities are related to these through Eqs. (2.11, 2.12, 2.13). Plots and features of the amplitudes are given in the next section.

Characteristic values of the differential and integrated cross sections for the 7 TeV

data given by this representation are

$$\begin{aligned}
\sigma_{\text{el.}} &= 25.5418 \text{ mb} ; \sigma_{\text{inel.}} = 73.1082 \text{ mb} ; \sigma_{\text{el.}}/\sigma = 0.2589 ; \\
|t|_{\text{dip}} &= 0.4847 \text{ GeV}^2 ; (d\sigma/dt)_{\text{dip}} = 0.01532 \text{ mb GeV}^{-2} ; \\
|t|_{\text{bump}} &= 0.6488 \text{ GeV}^2 ; (d\sigma/dt)_{\text{bump}} = 0.02816 \text{ mb GeV}^{-2} ; \\
\text{ratio}(\text{bump}/\text{dip}) &= 1.8383.
\end{aligned} \tag{3.3}$$

In a closeup examination of the graph, shown in the inset in Fig. 1, we observe a discontinuity in the magnitudes of $d\sigma/dt$ in the junction of the two sets of data. We estimate that a renormalization factor 0.86 would adjust the higher $|t|$ to the more forward data in this region.

It is very interesting to compare the 7 TeV data with the similar behavior of the 52.8 GeV data [8], that are available in the ranges $0.107 \times 10^{-2} \leq |t| \leq 0.5546 \times 10^{-2} \text{ GeV}^2$ with 34 points and $0.825 \leq |t| \leq 9.75 \text{ GeV}^2$ with 63 points. This comparison is shown in Fig. 2 and in Tables I and II, and the behavior of the amplitudes is discussed in Sec. IV.

IV. AMPLITUDES

The amplitudes obtained in the analysis of the data, based on Eqs. (2.7, 2.8), are shown in Fig. 3 and numerical information is given in Tables I and II. Their general features are common to the lower energies from ISR and the Tevatron, with regular variation of the parameters. The results agree with requirements from dispersion relations for amplitudes and for slopes [5], and the Coulomb interference accounts for the necessary generalization of the Coulomb phase, presented in the Appendix. Near $t \simeq 0$, the real part obeys the theorem by A. Martin [9] about its first zero, decreasing quickly and crossing zero at small $|t|$, before the imaginary part becomes small. The $|t|$ dependence of the amplitudes for all $|t|$ is shown in part (b) of Fig. 3. The imaginary part starts dominant over the real part, crosses zero at higher $|t|$, then remains negative and asymptotically tends to zero from the negative side, while the real part crosses zero again near $|t| = 0.8 \text{ GeV}^2$, becoming positive. After the second real zero, namely for $|t|$ larger than about 1.0 GeV^2 , the real amplitude stays positive, without further oscillation, and for $|t| \geq 2 \text{ GeV}^2$ becomes increasingly dominant over the imaginary part. Important qualitative feature of our description

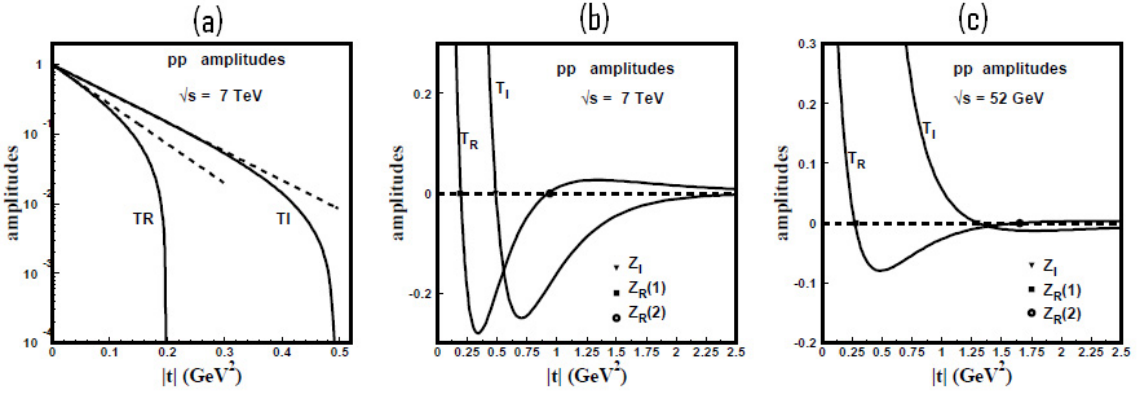


FIG. 3: (a) Forward scattering amplitudes T_R and T_I at $\sqrt{s} = 7$ TeV in log scale, normalized to one at $|t| = 0$, showing their slopes, $B_I = 19.77$ and $B_R = 30.2 \text{ GeV}^{-2}$, and their curvatures, and indicating positions of the first zeros $Z_R(1)$ and Z_I ; (b) Long t dependence of the real and imaginary scattering amplitudes showing the complete set of zeros; (c) t dependence of the real and imaginary scattering amplitudes at $\sqrt{s} = 52.8$ GeV. Comparing with the figure for 7 TeV, we observe that all zeros move towards smaller $|t|$ values as the energy increases.

of the data is that for large $|t|$ the magnitude of the imaginary part is smaller than the positive real part.

This behavior is consistent to a regular continuation of the results obtained for the ISR energies, and as an example we show in part (c) of Fig. 3 the amplitudes for 52.8 GeV. At this and higher energies [4] the Z_I zero occurs between $Z_R(1)$ and $Z_R(2)$. The magnitude of $T_I(s, t)$ is in general dominant over the real part between $Z_R(1)$ and $Z_R(2)$, so that the dip is located near Z_I . As the energy varies, while the first zero of $T_R(s, t)$ stays almost constant in the $|t|$ range from 0.15 to 0.3 GeV^2 , the positions of both Z_I and $Z_R(2)$ move to the left. The relative proximity of real and imaginary zeros influences the shape and depth of the dip. At 540 and 1800 GeV the imaginary zero is distant from both real zeros, so that no dip is formed, and only an inflection is observed.

Table II gives the positions of the zeros of the amplitudes and the characteristic observable quantities in pp elastic scattering at 7 TeV and 52.8 GeV.

The details of the dip-bump structure carry information on the scattering amplitudes, and are particularly sensitive to their relative behavior near their zeros [4]. Thus, a marked dip appears when one of the amplitudes (real or imaginary) crosses

TABLE II: Positions of zeros of the amplitudes, locations of the predicted dip and bump, and ratio characterizing the shape of this structure. For comparison that shows the regularity, we give the same information for $\sqrt{s} = 52.8$ GeV. We observe that as the energy increases all zeros move towards smaller $|t|$, with the imaginary zero moving faster, becoming more distant from the the second real zero $Z_R(2)$ and closer to the first one $Z_R(1)$.

\sqrt{s} GeV	Z_I GeV ²	$Z_R(1)$ GeV ²	$Z_R(2)$ GeV ²	$ t _{\text{dip}}$ GeV ²	$ t _{\text{bp}}$ GeV ²	$(d\sigma/dt)_{\text{dip}}$ mb/GeV ²	$(d\sigma/dt)_{\text{bp}}$ mb/GeV ²	ratio bp/dip	σ_{el} mb	σ_{inel} mb	$\sigma_{\text{el}}/\sigma$
52.8	1.3083	0.2710	1.6157	1.3560	1.7947	1.9×10^{-5}	6.3×10^{-5}	3.2805	7.4308	35.0591	0.1749
7000	0.4671	0.1641	0.8235	0.4847	0.6488	0.0153	0.0282	1.8383	25.54	73.11	0.26

the zero in the interval where the other amplitude stays nearly constant with magnitude small compared to the variation of the former. In a domain where one of the amplitudes is dominant, the zero of the amplitude with smaller magnitude does not affect the observable differential cross section, as happens in the region of the first real zero ($\approx 0.15 - 0.3$ GeV²).

The parts $d\sigma^R/dt$ and $d\sigma^I/dt$ of the differential cross section due to the real and imaginary amplitudes are shown in Fig. 4.

Differently from lower energies, the dip at $|t| \approx 0.5$ GeV² is more influenced by the proximity of the imaginary zero (≈ 0.5 GeV²) and the first real zero $Z_R(1)$ (at 0.2 GeV²). Due to the increasing proximity of the imaginary and real zeros at higher energies, the dip/bump structure becomes more marked, and this is expected to happen at 14 TeV.

At 7 TeV the bump that follows the dip is formed by the T_I and the T_R amplitude that have there similar magnitudes, with T_I becoming more strongly negative while T_R quickly becomes zero. This explains the ratio nearly 2 (actually 1.838) between bump and dip heights. After the bump the fall is faster because it is only determined by the dominant magnitude of the imaginary amplitude, that decreases fast in $|t|$. T_R is small positive, but of long range, surviving until it meets the expected perturbative tail after $|t| = 2$ GeV².

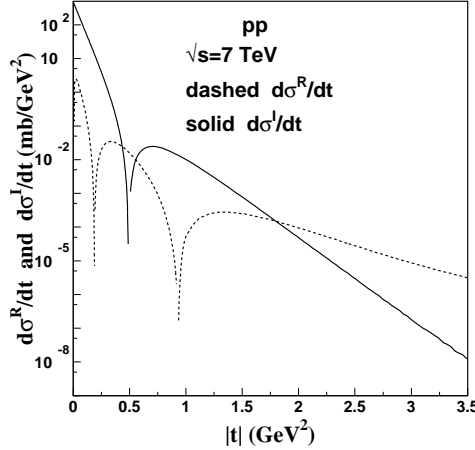
A. Forward scattering

The above description basically characterizes our results of the analysis of all TOTEM data at 7 TeV, but the forward scattering part deserves a more detailed analysis, because the data in this domain have higher precision and are crucial for the determination of the total cross section.

To study separately the forward data investigating the use of amplitudes with the exponential forms of Eq. (2.15), we select a set of the first 40 points in the interval $0.00515 \leq |t| \leq 0.0907 \text{ GeV}^2$. This forward set is used to compare the full-t analytic form described above with forward scattering analyses using exponential forms. Our analysis with Eqs. (2.7) and (2.8), with the parameters given in Eqs. (3.1) and (3.2), describes the forward set of 40 points with an average squared deviation $\langle \chi^2 \rangle = 0.1062$.

On the other hand, with Eq. (2.15) and the forward scattering parameters suggested

FIG. 4: Partial cross sections $d\sigma^I/dt$ and $d\sigma^R/dt$ as functions of $|t|$ as calculated with the analytic forms of Eqs. (2.7) and (2.8). The dip in the sum $d\sigma/dt$ (at 0.485 GeV^2) is close to the zero of the imaginary part (at 0.467 GeV^2).



by the TOTEM Collaboration[2]

$$\begin{aligned}\sigma &= 98.58 \pm 2.23 \text{ mb}, \quad \rho = 0.141 \pm 0.007, \\ B_I &= 19.89 \pm 0.27 \text{ GeV}^{-2}, \quad B_R = B_I,\end{aligned}\tag{4.1}$$

we find $\langle \chi^2 \rangle = 0.1129$ for this set of 40 points.

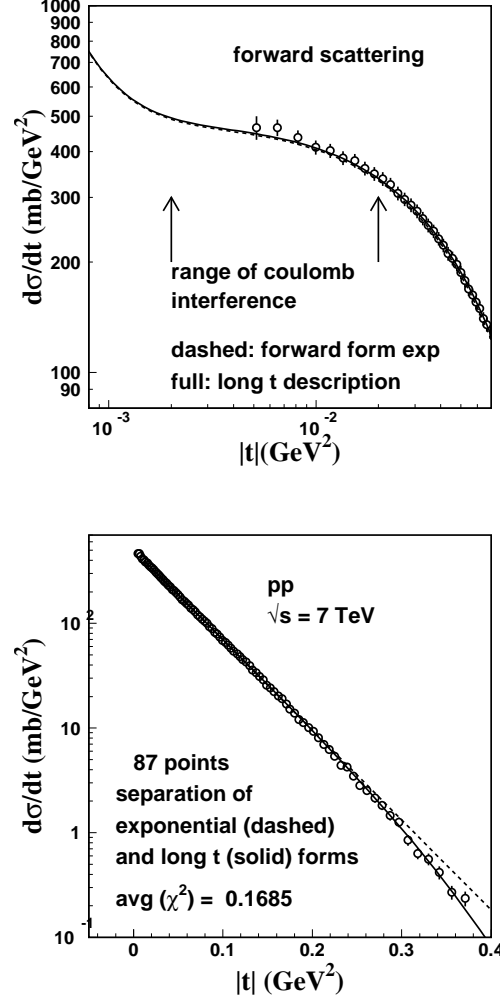
As a curiosity, we tested the pure exponential forms for the set of 40 points, using the values of σ , ρ , B_I , B_R given in Eq. (3.1), remarking that they are obtained in the all- t analysis. We then obtain an average $\langle \chi^2 \rangle = 0.1034$, which may even appear as a better description (actually, we can only say not worse) than obtained with the numbers of Eq. (4.1).

Of course there is no statistical significance in these differences of $\langle \chi^2 \rangle$ values, and visually these representations are almost degenerated as shown in part (a) of Fig. 5. The importance of the construction of the full- t analytical forms is that they are physically more realistic, including curvatures, magnitudes, signs, zeros of the two amplitudes, reflecting important information of the collision dynamics. In particular, one should remind that the usual treatment of data with $B_R = B_I$ is essentially wrong, although it is used in practice because ρ is small. In fact, the slope B measured directly in $d\sigma/dt$ is related to the slopes of the amplitudes through

$$B = \frac{B_I + \rho^2 B_R}{1 + \rho^2}.\tag{4.2}$$

Therefore, the expected difference between values is approximately $B_I \approx B - 0.1 \text{ GeV}^{-2}$. However, such a simplification hides important properties of the dynamics. Furthermore, since $d\sigma/dt$ is not a pure exponential form $A e^{-B|t|}$, determinations of σ made with this approximation carry an intrinsic error. The scattering amplitudes must have zeros, consequently the slopes of the real and imaginary amplitudes are t dependent, deviating from pure exponential forms. So, the determination with high precision of total cross-section, ρ and slopes cannot be free from model-dependence, and differences are sensitive unless the measurements reach very small $|t|$. Such a limitation of the approximation is shown in part(b) of Fig. 5, where we exhibit the long- t and the exponential solutions in the presence of the 87 points of the first part of TOTEM measurements, with $|t| \leq 0.371 \text{ GeV}^2$. A pure exponential form (dashed line) appears as if it is adequate (visually, and within errors) within the range $|t| < 0.25$, but in reality the real part has a zero and becomes negative. We here stress that the physical quantities σ , ρ , B_I and B_R are obtained as lim-

FIG. 5: (a): Data and analytic representation for elastic pp scattering at 7 TeV in the forward range. Solid and dashed curves represent respectively the long-t solution and the exponential forms of Eq. (??) with parameters of Eq. (4.1) given by the experimentalists; (b) : The same functions are drawn together with the 87 points of first part of TOTEM data, showing the separation of exponential and full-t forms as $|t|$ becomes large.



iting values as $|t| \rightarrow 0$ from a complex amplitude, thus requiring a basic analytical form. Therefore, they are naturally model-dependent, particularly if the data do not get close to the origin. It is thus very meaningful that the numerical values in Eqs. (3.1) and (4.1) are compatible. Note that our analytic representation for the amplitudes covers the whole t region with the same accuracy, and contains more physical information than a mere exponential fit. Naturally, the distinction between the two proposed descriptions for $d\sigma/dt$, and consequently for the values of σ (98.65

and 98.58 mb) would require high precision in the measurements. For example, for $|t| = 5 \times 10^{-3} \text{ GeV}^2$ the predicted values for $d\sigma/dt$ are 447.2 and 444.8 mb/GeV² respectively.

B. Universality of the perturbative three gluon amplitude at 7 TeV

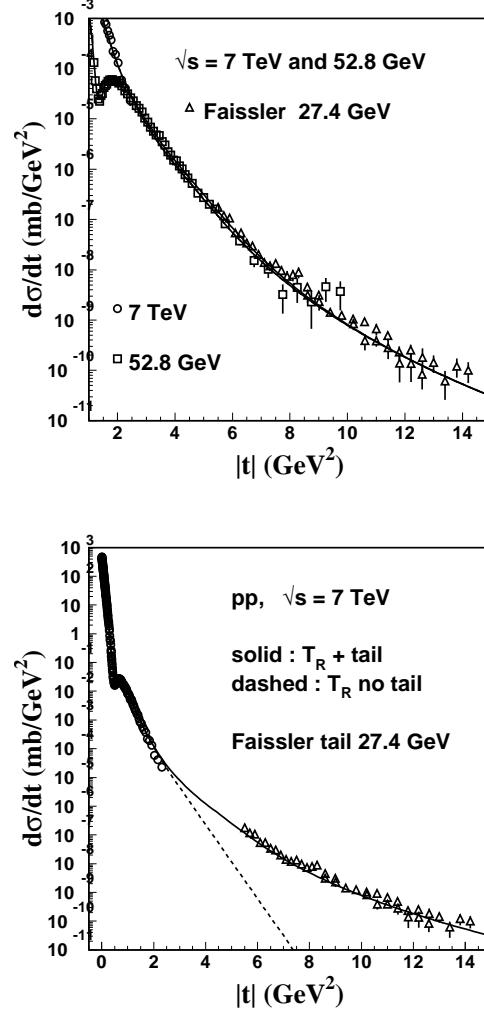
At energies above $\sqrt{s} \approx 20 \text{ GeV}$, a perturbative term due to three-gluon exchange, energy independent and of magnitude 10^{-7} to $10^{-11} \text{ mb/GeV}^2$, produces a tail of form $|t|^{-8}$ that dominates the scattering cross sections at large $|t|$. This term that was observed in Faissler experiment at 27.4 GeV [6], is real positive for pp and negative for $p\bar{p}$. In pp scattering at 52.8 GeV, where data exist up to $|t| \approx 10 \text{ GeV}^2$, the matching of the data and the tail is perfect and shows that the real amplitude at intermediate $|t|$ values, namely after the dip in the cross section, should actually be positive, in agreement with our description of the amplitudes.

In our approach, the non-perturbative contributions vanish fast for large $|t|$, and we expect that for $|t| \gg 3 \text{ GeV}^2$, the cross sections at all energies behaves like

$$d\sigma/dt \approx (\hbar c)^2 [R_{ggg}(t)]^2 \approx 0.08 t^{-8} \text{ (mb/GeV}^2\text{)} . \quad (4.3)$$

Fig. 6 shows part of the 52.8 GeV and 7 TeV data, together with the points of the 27.4 GeV tail at large $|t|$. The superposition of points observed starting at $|t| = 2 \text{ GeV}^2$ leads to the feeling that with extended data the universal tail would be observed at 7 TeV, similarly to the behavior seen at lower energies. The second part of the figure shows the expected smooth connection of the TOTEM data at 7 TeV to the 27.4 GeV tail data points, according to the construction of the amplitudes described above. The $|t|$ distribution is expected to reach the three-gluon-exchange tail in the range from 5 to 15 GeV². Unfortunately the experimental data end a little before, but observing the figure we are lead to believe that the present data are pointing towards the tail. Since $T_R(t)$ and the tail are positive, there will be no marked structure caused by cancellation, as expected to occur in $p\bar{p}$. At large $|t|$ the cross section will be of form $1/|t|^8$, according to the perturbative three-gluon exchange tail. The superposition between T_R and the perturbative tail may provide precious information about the non-perturbative regime. The real tail, with known sign, magnitude and shape, provides a reference basis, analogous to what

FIG. 6: (a) Prediction for the observation of the large $|t|$ tail (triangles) at 7 TeV, based on the comparison with the data at 52.8 GeV. The solid line is our solution for 7 TeV data with the tail added in the real part amplitude. In part (b) the dashed line is our solution without the perturbative tail.



the Coulomb interaction does at small $|t|$, important for the identification of the amplitudes.

C. Impact Parameter Form for the Amplitudes

As mentioned before, our amplitudes given as functions of the momentum transfer $|t|$ by Eqs. (2.7, 2.8) are written in impact parameter space through the Fourier

transforms

$$\tilde{T}_K(s, b) = \frac{1}{2\pi} \int d^2\vec{q} e^{-i\vec{q}\cdot\vec{b}} T_K^N(s, t = -q^2)$$

where $K = I$ and $K = R$ in $\tilde{T}_K(s, b)$ refer to the real and imaginary parts . They are given in analytical forms by

$$\tilde{T}_K(s, b) = \frac{\alpha_K}{2\beta_K} e^{-\frac{b^2}{4\beta_K}} + \lambda_K \tilde{\psi}_K(s, b) ,$$

where

$$\tilde{\psi}_K(s, b) = \frac{2 e^{\gamma_K}}{a_0} \frac{e^{-\sqrt{\gamma_K^2 + \frac{b^2}{a_0}}}}{\sqrt{\gamma_K^2 + \frac{b^2}{a_0}}} \left[1 - e^{\gamma_K} e^{-\sqrt{\gamma_K^2 + \frac{b^2}{a_0}}} \right]$$

is the shape function in b space. Use has been made of the integration formula [4, 10]

$$\int_0^\infty J_0(\beta v) \frac{e^{-\lambda\sqrt{1+v^2}}}{\sqrt{1+v^2}} v dv = \frac{e^{-\sqrt{\lambda^2+\beta^2}}}{\sqrt{\lambda^2+\beta^2}} . \quad (4.4)$$

Fig. 7 shows the parts $\tilde{T}_K^{(\text{exp})}(s, b)$ and $\tilde{T}_K^{(\text{shape})}(s, b)$ corresponding respectively to the terms in exponential and shape function of the amplitudes in $|t|$, and Fig. 8 shows their sums. The shape functions are zero at $b = 0$ and all parts are positive for all b . The amplitude in b -space can be put in the form

$$\tilde{T}_R(s, b) + i\tilde{T}_I(s, b) = i\sqrt{\pi} [1 - e^{2i\delta(s, b)}] \quad (4.5)$$

with real $\delta(s, b)$.

The Fourier transform $\tilde{R}_{gg}(s, b)$ of the perturbative tail is shown in Fig. 9. Its behavior is of a form approximated like $\tilde{R}_{gg}(s, b) \approx 0.0022 J_0(c b)/(1 + (d b)^2)$, with $c \approx 1.863$ and $d \approx 4.0$ in GeV.

D. Comparison with the amplitudes in the BSW model

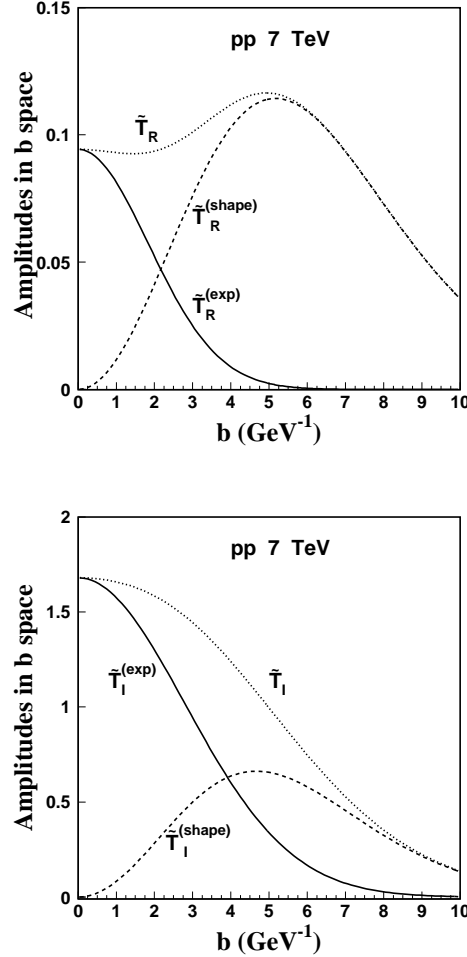
Since the behavior of the amplitudes gives physical information on the collision dynamics and its determination is model dependent, it is important to compare our results with other models that describe elastic pp and $p\bar{p}$ scattering processes [11–15]. Results on amplitudes that can be directly compared with ours are given by the model proposed by Bourrely, Soffer and Wu (hereafter referred to as BSW model) [11]. We find important similarities and differences which we discuss below.

The BSW model leads to values for the imaginary and real slopes with $B_R > B_I$ (as expected), to a first real zero at small $|t|$ (as expected) and to a first imaginary zero

near the cross section dip (as expected) and to a second real zero at intermediate $|t|$. These are the first basic, but crucial qualitative agreements with our approach. There also exist several quantitative and qualitative differences that may reflect important physical information behind the observables. In Fig. 10 we compare details of cross section (part (a)) and of amplitudes (part(b)).

In the very forward region, the two descriptions cross each other, leading to different values at the optical point (with total cross section 92.33 mb in BSW and 98.65 mb for us) ; the slopes are qualitatively similar, with stronger B_R leading to a first real zero at low $|t|$ in both cases, as expected by Martin's theorem.

FIG. 7: (a) and (b) : respectively real and imaginary parts of the amplitude in impact parameter space , showing separately the contributions from the exponential (Gaussian form, solid) and shape functions (dashed) of the original amplitudes, and their sum (dotted).



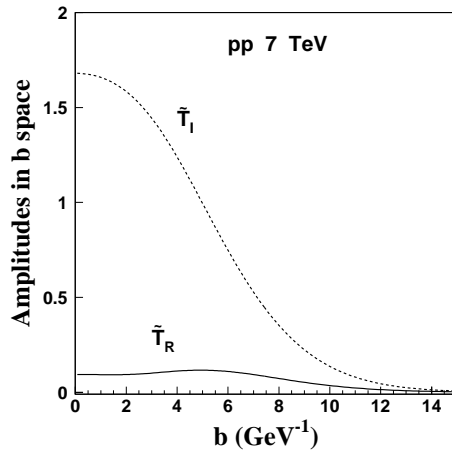
In the intermediate domain ($0.3 < |t| < 2$) that includes the dip-bump region, the BSW cross section overshoots the experimental data and our results by a factor of nearly 2, caused by excessive magnitudes of both real and imaginary amplitudes in this region.

The location of the dip-bump structure is also slightly shifted to a larger $|t|$ and our dip is sharper than that of BSW. For $|t| \simeq 2.5 \text{ GeV}^2$, BSW and ours approximate each other, but this is rather a coincidence as we can see from the behavior of the amplitudes.

After the first zeros, the BSW amplitudes have larger magnitudes, and the second real zero is shifted to larger $|t|$ compared to ours, and this has influence in the dip-bump shape. Near the first zero of the imaginary amplitude, the BSW real amplitude is about 70% larger than ours in magnitude.

Characteristic quantities of the BSW results are $\sigma = 92.33 \text{ mb}$, $B_I = 19.3 \text{ GeV}^{-2}$, $B_R = 25.8 \text{ GeV}^{-2}$, $\rho = 0.126$, to be compared to the values given in Table I. In the range of interest their amplitudes have two real zeros, at 0.205 and 1.475 (a third real zero is farther away), and three imaginary zeros at 0.525, 2.705 and 6.265 ; in our case there are two (and only two) real zeros, both more to the left, and

FIG. 8: Real and imaginary parts of the amplitude in impact parameter coordinate.

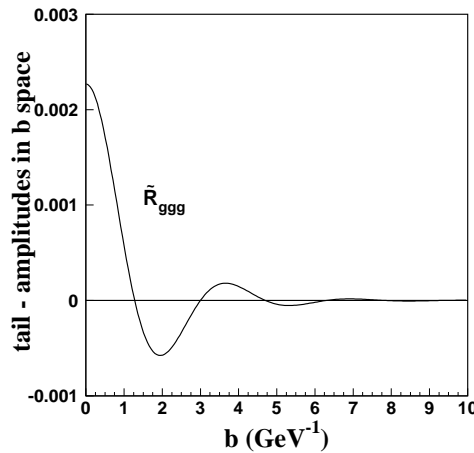


only one imaginary zero, also at smaller $|t|$.

Although the quantitative differences are important, it is impressive the similarity in the forms of the amplitudes in the two calculations in range of the data, up to 2.5 GeV^2 . This is the range where we believe that the non-perturbative dynamics is dominant and where eikonal-based models are expected to be valid.

Important qualitative differences between ours and BSW model is in the behavior of amplitudes for large $|t|$ values ($|t| \gtrsim 2 \text{ GeV}^2$), which is illustrated in the up-right corner inset of Fig.10-(b) in the form of partial contribution to the cross section. In our model (solid for real and dash-dotted for imaginary), the non-perturbative amplitudes falls off exponentially for large $|t|$ and the the real part is made dominant with the action of the perturbative three-gluon exchange term (dotted). In BSW, the amplitudes fall rather slowly, and exhibit further zeros. Contrary to our approach, BSW cross section is dominated by the imaginary part for large $|t|$. Due to the presence of the second zero, there appears a slight inflection at $|t| \sim 3 \text{ GeV}^2$. Interestingly such inflection also appears in our model coincidentally by a completely different reason, due to the perturbative real amplitude summing to the real amplitude. It seems that $\sqrt{s} = 52 \text{ GeV}$ data supports strongly the contribution of this

FIG. 9: Representation of the amplitude for the perturbative tail in b space.



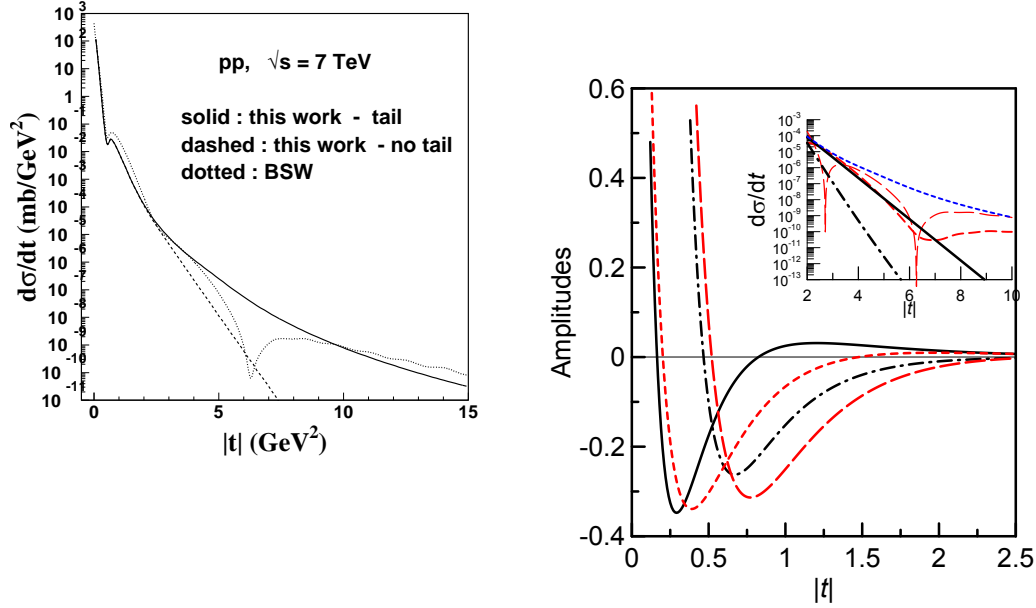


FIG. 10: (a) Comparison of $d\sigma/dt$ at 7 TeV in our description (solid line) and in BSW model [11] (dash-dotted line). In the large $|t|$ range our non-perturbative amplitudes fall exponentially (dashed line) and the universal (for all energies) real three-gluon tail enters to dominate the scattering. In the BSW case a second imaginary zero at $|t| \approx 2.7 \text{ GeV}^2$ causes no mark, because the real part is not small, and a third zero in the imaginary amplitude predicts a marked dip at $|t| \approx 6.3 \text{ GeV}^2$. (b) Comparison of amplitudes. Solid and dash-dotted lines are the real and imaginary amplitudes of our representation, while dashed and long-dashed lines are those of BSW. In the inset at up-right corner, we show the large $|t|$ behaviour of amplitudes in terms of partial differential cross sections. Our amplitudes fall exponentially to zero (solid and dash-dotted for non-perturbative real and imaginary contributions, respectively), giving room for the perturbative contributions (dotted) similarly to observations at lower collision energies.

three-gluon exchange amplitude.

These above differences between BSW and our model lead to significant differences in the expectations for 14 TeV. In our case, we use the smoothness in the energy dependence of the parameters and of the characteristic features of the amplitudes to obtain a prediction for the higher energy. This shows a more pronounced dip-bump structure, which appears at a little bit smaller $|t|$. This is due to the zero of the

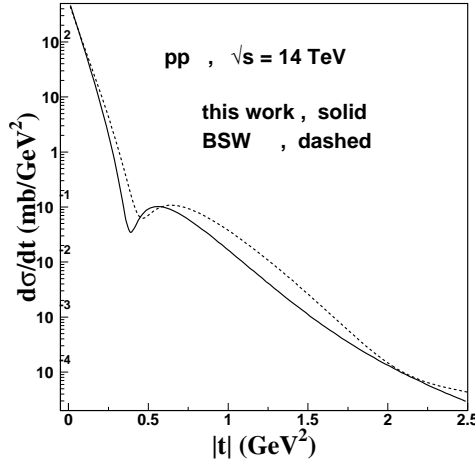


FIG. 11: Comparison of predictions for 14 TeV , where the dip/bump structure becomes more pronounced.

imaginary part, pinched by the two zeros of real part which are both approaching the imaginary zero for large \sqrt{s} . In Fig.11, we compare the two predictions, which are quite different in the behavior of dip-bump structure, as well as in the large $|t|$ behavior.

V. SUMMARY AND DISCUSSION

In this paper we present an analysis of the recent TOTEM data for the elastic scattering cross section at $\sqrt{s} = 7$ TeV, extending method employed at lower (ISR and Fermilab) energies [4]. The central point of our approach is that we describe the differential cross section directly in terms of scattering amplitudes, expressed analytically for all observed $|t|$ domain, together with the contribution from the perturbative three-gluon exchange process at large $|t|$. Differently from a mere parameterization fit of the differential cross section, our approach offers a qualified interpretation of data in terms of amplitudes, intending to serve as a bridge between data and theoretical descriptions by dynamical models.

For example, it is fundamental to recognize the difference of the slope parameters of real and imaginary amplitudes to describe the all $|t|$ domain, although, due to the small value of the ρ parameter the effect is not clearly visible while looking only at the forward scattering data. Furthermore, our analytic representation also can be written explicitly in the impact parameter space, that may permit us to discuss the physical meaning of our parameters in terms of geometrical models.

Our approach works perfectly well for $\sqrt{s} = 7$ TeV , giving an excellent representation for the data, including the forward region, and covering the dip at $|t| \approx 0.5 \text{ GeV}^2$ and the subsequent bump. The analysis leads to a description of the dip/bump structure of the differential cross section in terms of positions of zeros and magnitudes of the real and imaginary amplitudes.

At 7 TeV the zero of T_I and the dip nearly coincide, at about 0.5 GeV^2 , so that the height of the dip gives the magnitude of T_R in this region. In the bump region after the dip, the magnitudes of the real and imaginary parts become similar, so that the form of the subsequent bump structure depends very sensitively on the interplay of the two amplitudes. The maximum of the bump occurs where the magnitudes of the real and imaginary amplitudes are nearly equal. With this behavior, the ratio bump/dip = 1.84 is nearly 2 .

The gap in energy of the experiments at 7 TeV and the energies accessed in the long history of pp and p \bar{p} scattering is enormous. Nevertheless, elastic (soft) processes are very conservative, with smooth energy dependences, so that we are able to transfer to this higher energy the experience, methods and knowledge acquired before. The zeros of the amplitudes determined from the present analysis (one imaginary zero and two real zeros) are consistent as natural extension of the previous work for lower energies. Since the behavior of the free parameters is smooth, we can extend the present analysis to the future $\sqrt{s} = 14$ TeV experiment. We foresee that there will be a clear dip at $t \simeq 0.45 \text{ GeV}^2$ with similar bump structure with ratio ≈ 3 and a total cross section $\sigma \simeq 108 \text{ mb}$. This description concerns the non-perturbative regime characteristic of elastic and diffractive scattering (including multi-pomeron and reggeon exchanges).

It also becomes clear that the assumption, introduced and discussed by Donnachie and Landshoff [7] on the universality of the three gluon exchange amplitude, observed at 27.4 GeV [6] and higher ISR energies, is still consistent with the 7 TeV data,

that likely are pointing to the distant tail, as seen in Fig. 6. If this assumption is true, some very interesting consequences can be drawn. First, for $|t| \gg 3 \text{ GeV}^2$, the scattering amplitude is dominated by this process and consequently the imaginary part should be small, while the magnitude and sign of the real part is determined by Eq. (2.14). Although the present analysis already indicates the consistency of this assumption, the precise behavior of the amplitudes in the transition region from non-perturbative to perturbative dynamics may be affected sensitively by the data in this region. Therefore, it is extremely important to confirm this behavior at $\sqrt{s} = 7 \text{ TeV}$ by extending TOTEM analysis to higher $|t|$ values, with consequences for the identification of the amplitudes in the range of transition. If $d\sigma/dt$ is found to follow the tail without marked structure, we can conclude that in this region the real amplitude has positive sign and that the imaginary part has much smaller magnitude. It would be nice to reach more extended $|t|$ ranges and high precision in this new era of studies of high energy collisions.

It is interesting to remark that in the $p\bar{p}$ case, the negative perturbative term may produce a third zero in the real amplitude causing a dip in the $|t|$ distribution. This could have been seen in Fermilab data at 540 and 1800 GeV if the measurements had reached high enough $|t|$ values.

In Subsec. IV D we compare several aspects of our work with the results of a specific model [11], showing important similarities and differences.

To conclude, working with a specific analytical form for the amplitudes, we have produced a detailed and precise description of the data of elastic pp scattering at 7 TeV. The knowledge of the individual amplitudes carries more physical information on the dynamics of the scattering processes, and this work is part of an effort to find a consistent description of the amplitudes covering regularly the data for all energies in the whole t - range [4]. The present analysis of the TOTEM data reproduces accurately the behavior of the observed cross section in the whole t -range, with consistent proposal for the determination of the amplitudes, confirming the expectations of similarity with lower energies. It is hoped that this description can be successfully extended to the future measurements higher energies.

VI. APPENDIX: THE COULOMB PHASE

Here we derive an expression for the Coulomb interference phase appropriate for forward scattering amplitudes with $B_R \neq B_I$.

The starting point is the expression for the phase obtained by West and Yennie [16]

$$\Phi(s, t) = (-/+)\left[\ln\left(-\frac{t}{s}\right) + \int_{-4p^2}^0 \frac{dt'}{|t' - t|} \left[1 - \frac{F^N(s, t')}{F^N(s, t)}\right]\right], \quad (6.1)$$

where the signs $(-/+)$ are applied to the choices $pp/p\bar{p}$ respectively. The quantity p is the proton momentum in center of mass system, and at high energies $4p^2 \approx s$.

For small $|t|$, assuming that $F^N(s, t')$ keeps the same form for large $|t'|$ (this approximation should not have practical importance for the results), we have

$$\begin{aligned} \frac{F^N(s, t')}{F^N(s, t)} &= \frac{F_R^N(s, 0)e^{B_R t'/2+i} F_I^N(s, 0)e^{B_I t'/2}}{F_R^N(s, 0)e^{B_R t/2+i} F_I^N(s, 0)e^{B_I t/2}} \\ &= \frac{c}{c+i} e^{B_R(t'-t)/2} + \frac{i}{c+i} e^{B_I(t'-t)/2}, \end{aligned} \quad (6.2)$$

where

$$c \equiv \rho e^{(B_R - B_I)t/2}. \quad (6.3)$$

The integrals that appear in the evaluation of Eq. (6.1) are reduced to the form [17]

$$I(B) = \int_{-4p^2}^0 \frac{dt'}{|t' - t|} \left[1 - e^{B(t'-t)/2}\right], \quad (6.4)$$

that is solved in terms of exponential integrals [18] as

$$\begin{aligned} I(B) &= E_1\left[\frac{B}{2}(4p^2 + t)\right] - E_i\left[-\frac{Bt}{2}\right] + \ln\left[\frac{B}{2}(4p^2 + t)\right] \\ &+ \ln\left[-\frac{Bt}{2}\right] + 2\gamma. \end{aligned} \quad (6.5)$$

The real and imaginary parts of the phase are then written

$$\Phi_R(s, t) = (-/+)\left[\ln\left(-\frac{t}{s}\right) + \frac{1}{c^2 + 1} \left[c^2 I(B_R) + I(B_I)\right]\right], \quad (6.6)$$

and

$$\Phi_I(s, t) = (-/+)\frac{c}{c^2 + 1} \left[I(B_I) - I(B_R)\right]. \quad (6.7)$$

With σ in mb and t in GeV^2 , the practical expression for $d\sigma/dt$ in terms of the parameters σ , ρ , B_I and B_R is

$$\begin{aligned} \frac{d\sigma}{dt} &= \pi (\hbar c)^2 \left[\left[\frac{\rho \sigma e^{B_R t/2}}{4\pi (\hbar c)^2} + F^C e^{\alpha \Phi_I} \cos(\alpha \Phi_R) \right]^2 \right. \\ &\quad \left. + \left[\frac{\sigma e^{B_I t/2}}{4\pi (\hbar c)^2} + F^C e^{\alpha \Phi_I} \sin(\alpha \Phi_R) \right]^2 \right]. \end{aligned} \quad (6.8)$$

At high energies and small $|t|$ we simplify

$$4p^2 + t \rightarrow s$$

and then the functional form of $I(B)$ is written

$$I(B) = E_1\left(\frac{Bs}{2}\right) - E_i\left(-\frac{Bt}{2}\right) + \ln\left(\frac{Bs}{2}\right) + \ln\left(-\frac{Bt}{2}\right) + 2\gamma . \quad (6.9)$$

For large s , the term $E_1(Bs/2)$ can be neglected, and the phase becomes insensitive to s .

We may recall the usual expression from West and Yennie

$$\alpha\Phi_{WY} = (-/+)\alpha\left[\gamma + \ln\left(-\frac{Bt}{2}\right)\right] \quad (6.10)$$

that can be obtained from Eq. (6.6) with $B_R = B_I = B$ and using the low t behaviour

$$E_i\left[-\frac{Bt}{2}\right] \approx \gamma + \log -\frac{Bt}{2} .$$

To stress the influence of the calculation with different slopes, a numerical comparison is presented in Fig. 12, where we choose *high* unrealistic parameter values $\rho = 0.3$ and $B_R/B_I = 5$ to enhance differences, and the lines are drawn for $B_I = 15 \text{ GeV}^{-2}$, with the $d\sigma/dt$ slope B of the WY formula taken as given by Eq. (4.2)

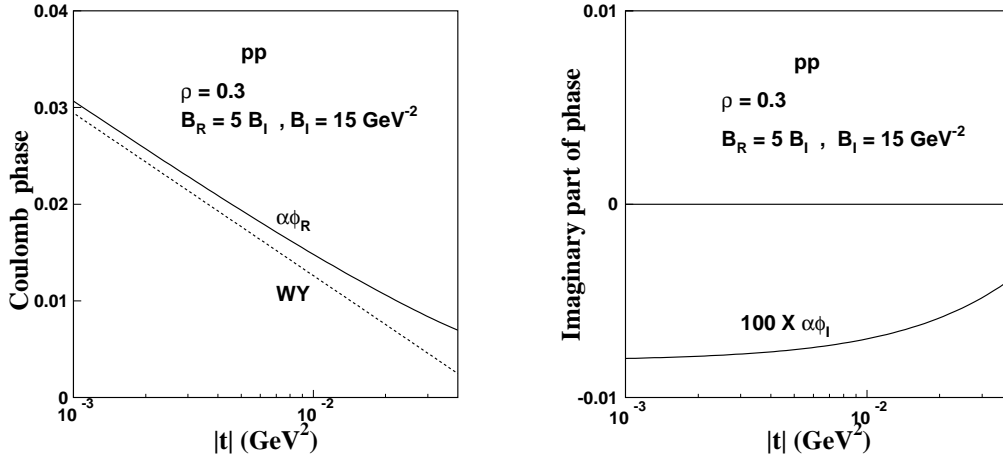
$$B = \frac{\rho^2 B_R + B_I}{1 + \rho^2} . \quad (6.11)$$

The plot of $\alpha\Phi_I(s, t)$ in the second part of Fig. 12 shows that its values are extremely small so the the imaginary part of the phase can be safely put equal to zero.

The construction of the Coulomb phase has been studied in the eikonal formalism appropriate for the interference of Coulomb and nuclear interactions [17, 19, 20] with special attention given to to the influence of the proton electromagnetic form factor. These treatments keep the assumption that the real part of the nuclear amplitude has the same slope as the imaginary part, and the results are not very different from the West Yennie formula. Some of these results have been tested against the data [21].

Fig. 13 shows the values of the Coulomb interference phase in the kinematical conditions of the 7 TeV LHC experiment. We show together the phase obtained

FIG. 12: Comparison of the Coulomb phase $\alpha\Phi_R$ from our calculation of Eq. (6.6) with the West-Yennie WY expression in Eq. (6.10). The unrealistic large values of parameters $\rho = 0.3$ and $B_R/B_I = 5$ are chosen in order to enhance differences. The calculation is made at $\sqrt{s}=50$ GeV, but the values of $\alpha\Phi_R(s, t)$ do not show explicit dependence on s up to the LHC energy. The plot of $\alpha\Phi_I$ in the RHS shows extremely small values (notice the scale), about 100 times smaller than $\alpha\Phi_R$, so that we can safely put $\alpha\Phi_I$ equal to zero in Eq.(6.8).



with the expression [19]

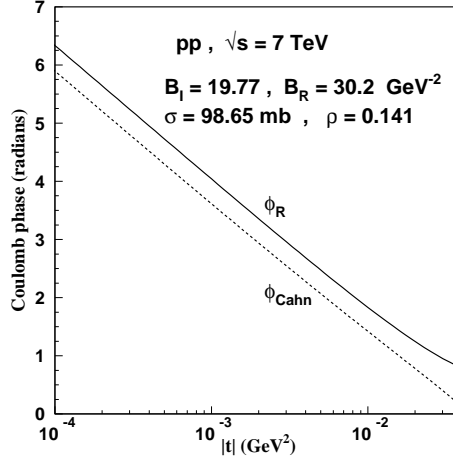
$$\begin{aligned} \Phi_{\text{Cahn}} = & -[\gamma + \ln(-Bt/2) + \ln(1 + 8/(B\Lambda^2))] \\ & + (-4t/\Lambda^2) \ln(-4t/\Lambda^2) - 2t/\Lambda^2] , \end{aligned} \quad (6.12)$$

where the proton form factor has been used with exponential form, $\Lambda^2 = 0.71 \text{ GeV}^2$, and B is taken as equal to B_I .

Acknowledgments

The authors are very grateful to the members of the Totem Collaboration, particularly to K. Osterberg, S. Giani and M. Deile, for offering an opportunity of presentation and discussion of the present work. The authors wish to thank CNPq,

FIG. 13: Values of the Coulomb interference phase evaluated in the kinematical conditions of pp elastic scattering at 7 TeV , with account made for the difference in the slopes of the real and imaginary amplitudes. For comparison we show the phase obtained with the basic formula [19] of Eq.(6.13)



PRONEX and FAPERJ for financial support. A part of this work has been done while TK stayed as a visiting professor at EMMI-ExtreMe Matter Institute/GSI at FIAS, Johann Wolfgang Universität, Frankfurt am Main. TK expresses his thanks to the hospitality of Profs. H. Stoecker and D. Rischke.

-
- [1] G. Antchev et al.(TOTEM Collaboration), *Europhys. Lett.* **95**, 41001 (2011); id *Europhys. Lett.* **96**, 21002 (2011).
 - [2] CERN-PH-EP-2012-239 and Durham Data Basis ; K. Eggert , talk at 2012 LHC Days, Split, Croatia, 1-6 October 2012 .
 - [3] H.G. Dosch, *Phys. Lett. B* **190**, 177 (1987) ; H.G. Dosch, E. Ferreira, A. Kramer *Phys. Rev. D* **50**, 1992 (1994) .
 - [4] E. Ferreira and F. Pereira, *Phys. Rev. D* **59** , 014008 (1998) ; *Phys. Rev. D* **61**, 077507 (2000).

- [5] E. Ferreira, *Int. Jour. Mod. Phys. E* **16**, 2893 (2007).
- [6] W. Faissler *et al.* *Phys. Rev. D* **23** (1981) 33 .
- [7] A. Donnachie, P. V. Landshoff, *Zeit. Phys. C* **2**, 55 (1979); *Phys. Lett. B* **387**, 637 (1996) .
- [8] E. Nagy *et al.* *Nucl.Phys. B* **150** (1979) 221 ; N. Amos *et al.* *Nucl. Phys. B* **262** (1985) 689 .
- [9] A. Martin, *Phys. Lett.B* **404**, 137 (1997).
- [10] S.Moriguchi *et al.* , "Mathematical Formulas III (Suugaku Koushiki III), Iwanami Zen-sho 244, Ed.10 (1971), p 201, Iwanami, Tokyo
- [11] C. Bourrely, J.M. Myers, J.Soffer and T.T. Wu , *Phys. Rev. D* **85**, 096009 (2012).
- [12] V. A. Petrov and A. V. Prokudin , *Eur. Phys. J. C* **23**, 135 (2002).
- [13] D.A.Fagundes, E.G.S. Luna, M.J. Menon and A.A. Natale , *Nucl. Phys. A* **886**, 48 (2012).
- [14] M.M. Islam, R.J. Luddy , A.V. Prokudin , *Int.J.Mod.Phys. A* **21** 21 (2006) 1 ; *Phys.Lett. B* 605 (2005) 115
- [15] L.L. Jenkovszky , A.I. Lengyel , D.I. Lontkovskyi *Int.J.Mod.Phys. A* **26** (2011) 4755
- [16] G. B. West and D. Yennie , *Ann. of Phys.* **3**, 190 (1958).
- [17] V. Kundrať and M. Lokajicek, *Phys. Lett. B* **611**, 102 (2005); V.Kundrať, M.Lokajicek and I. Vrocc, *Phys. Lett. B* **656**, 182 (2007).
- [18] M. Abramowitz and I. Stegun, *Handbook of Mathematical Functions*.
- [19] R. Cahn, *Zeit. Phys. C* **15**, 253 (1982) .
- [20] O. V. Selyugin , *Phys. Rev. D* **60**, 074028 (1999) .
- [21] V. A. Petrov, E. Predazzi and A. V. Prokudin , *Eur. Phys. J. C* **28**, 525 (2003).
- [22] Because the present data stops at about 2.5 GeV², the quantity β_R is difficult to fix uniquely.